NeuroImage 195 (2019) 272–284

Contents lists available at ScienceDirect

NeuroImage

journal homepage: www.elsevier.com/locate/neuroimage

It's the little things: On the complexity of planar electrode heating in MRI

Johannes B. Erhardt [a,c,h,1], Thomas Lottner [b,1], Jessica Martinez [c,e], Ali C. Özen [b,i], Martin Schuettler [d], Thomas Stieglitz [a,g,h], Daniel B. Ennis [f], Michael Bock [b,*]

[a] Department of Microsystems Engineering—IMTEK, University of Freiburg, Freiburg, Germany
[b] Department of Radiology - Medical Physics, Medical Center University of Freiburg, Faculty of Medicine, University of Freiburg, Freiburg, Germany
[c] Department of Radiology, University of California, Los Angeles, CA, USA
[d] CorTec GmbH, Freiburg, Germany
[e] Department of Bioengineering, University of California, Los Angeles, CA, USA
[f] Department of Radiology, Stanford University, Stanford, CA, USA
[g] Bernstein Center Freiburg, Freiburg, Germany
[h] BrainLinks-BrainTools, Freiburg, Germany
[i] German Cancer Consortium Partner Site Freiburg, German Cancer Research Center (DKFZ), Heidelberg, Germany

ARTICLE INFO

Keywords:
Magnetic resonance imaging
RF heating
Implants
Planar electrodes
ECoG
MR safety

ABSTRACT

Neurological disorders are increasingly analysed and treated with implantable electrodes, and patients with such electrodes are studied with MRI despite the risk of radio-frequency (RF) induced heating during the MRI exam. Recent clinical research suggests that electrodes with smaller diameters of the electrical interface between implant and tissue are beneficial; however, the influence of this electrode contact diameter on RF-induced heating has not been investigated. In this work, electrode contact diameters between 0.3 and 4 mm of implantable electrodes appropriate for stimulation and electrocorticography were evaluated in a 1.5 T MRI system. *In situ* temperature measurements adapted from the ASTM standard test method were performed and complemented by simulations of the specific absorption rate (SAR) to assess local SAR values, temperature increase and the distribution of dissipated power. Measurements showed temperature changes between 0.8 K and 53 K for different electrode contact diameters, which is well above the legal limit of 1 K. Systematic errors in the temperature measurements are to be expected, as the temperature sensors may disturb the heating pattern near small electrodes. Compared to large electrodes, simulations suggest that small electrodes are subject to less dissipated power, but more localized power density. Thus, smaller electrodes might be classified as safe in current certification procedures but may be more likely to burn adjacent tissue. To assess these local heating phenomena, smaller temperature sensors or new non-invasive temperature sensing methods are needed.

1. Introduction

1.1. Motivation

Implantable electrodes are increasingly used to restore normal function, in particular, in patients with neuro-degenerative diseases. In these patients, implantable electrodes can increase the quality of life while simultaneously providing diagnostic information about neuronal activity. Implantable electrodes are usually polymer substrates with linear or planar arrays of metal electrode contacts applied to the targeted tissue. Common applications of such here termed “electrodes” are electrical stimulation of the brain for Parkinson's patients, recording of the electrocorticogram (ECoG) for pre-surgical evaluation of epilepsy (Hermes et al., 2010), brain function mapping (Dykstra et al., 2012), and the implementation of neuroprosthetics (Ordonez et al., 2012). For these applications it is beneficial to accurately localize the electrode contacts with respect to the brain anatomy immediately after implantation.

The onset and progression of neuro-degeneration is often monitored with magnetic resonance imaging (MRI), as MRI provides an excellent soft tissue contrast and it can detect focal lesions in brain tissue without ionizing radiation. Furthermore, the localization of the electrodes is better done with MRI than with computed tomography (Yang et al., 2012). In particular, MRI can visualize grey and white matter with high contrast, it is more sensitive in the detection of post-operative

* Corresponding author. University Medical Center Freiburg, Dept. of Radiology Medical Physics, Killianstrasse 5a, 79106, Freiburg, Germany.
E-mail address: michael.bock@uniklinik-freiburg.de (M. Bock).
[1] These authors contributed equally to this work.

https://doi.org/10.1016/j.neuroimage.2019.03.061
Received 26 October 2018; Received in revised form 7 March 2019; Accepted 26 March 2019
Available online 29 March 2019

complications, and MR images can be easily co-registered to pre-implantation MRI. In addition, MRI provides neuro-functional examination methods to detect epilepsy foci that can be important for fundamental epilepsy therapy research (Carmichael et al., 2007; Hawsawi et al., 2017; Min et al., 2012). Although performing MRI exams for post-operative monitoring of patients with implanted electrodes would be highly desirable, the presence of the electrodes during MRI exposes the patient to a significant safety hazard. The radio frequency (RF) excitation fields employed in MRI can cause a significant temperature increase in tissue surrounding the AIMD electrodes (Kainz et al., 2002; Nitz et al., 2001; Shellock, 2000). This heating effect is especially pronounced in devices that contain elongated metal structures such as cables that interface with brain tissue (Erhardt et al., 2018; Yeung et al., 2002). Many different methods have been proposed to reduce RF-induced heating (Bottomley et al., 2010; Eryaman et al., 2015, 2011; Etezadi-Amoli et al., 2015; Krafft et al., 2006; Ladd and Quick, 2000; Yeung et al., 2002). Despite precautions incidents with severe adverse events have been reported in AIMD patients undergoing MRI exams (Henderson et al., 2005; Spiegel et al., 2003).

1.2. Implantable planar electrodes and the trend towards smaller electrode contact diameters

Implantable or subdural planar electrodes are made of flat polymer sheets where the comprised electrode contacts are in one plane. By contrast, depth electrodes (used to target deep structures) have a cylindrical geometry resulting also in cylindrical electrode contacts. Planar electrodes are further distinguished into electrode “strips” (or paddle electrodes) when elongated or “grids” when comprised by several lines of electrode contacts. Strips, as used in this study, are used in intracranial video-EEG monitoring in the pre-surgical workup of patients with refractory focal epilepsy. Further applications are cortex stimulation (Saitoh and Koichi, 2009), brain mapping (Pirotte et al., 2009), ECoG or microECoG recording (Gupta et al., 2014; Hamilton et al., 2017; Jiang et al., 2017), and spinal cord stimulation (Kemler et al., 2000). The dimension of the electrode-tissue interface here termed “electrode contact” is a key parameter for electrical stimulation and bioelectrical signal recording (Cogan, 2008). Electrode contacts in most clinical applications have large diameters on the order of millimeters that provide low impedance and hence low noise during recording. A large surface area is also beneficial for electrical stimulation as it offers a higher charge injection capacity. However, large electrode contacts come with side-effects such as a larger foreign body response and poor spatial recording selectivity. Recent findings showed that small electrode contacts (μECoG: ~1 mm contact diameter and below) provide very similar information on the brain state with respect to recorded signal frequency band and power (Jiang et al., 2018) as standard size electrode contacts (ECoG: 2.7 mm electrode contact diameter). While providing similar recording quality, smaller contacts permit the realization of grid electrodes with much higher contact density, which can provide a dramatic improvement on spatial recording selectivity (Chang, 2015; Muller et al., 2016). Even smaller electrode contacts with diameters on the order of several 100 μm feature higher spatial resolution, that enables the detection of high frequency oscillations in small nerve cell ensembles (Zijlmans et al., 2017). In research settings electrode contact diameters as low as 20 μm have been reported (Stieglitz et al., 2009) and small electrodes were fabricated with surface coatings to match the charge injection capacity of large electrode contacts (Boehler et al., 2015). So far, the influence of the electrode contact diameter on RF-induced heating during an MRI exam has not been investigated.

1.3. RF-induced heating near implants in MRI

The specific absorption rate (SAR, W/kg) is a measure for the absorbed electromagnetic power per mass of a given tissue. Theoretical expressions for SAR can be derived from the complex Poynting theorem which originates from the Maxwell equations (Jackson, 2012). Assuming a homogeneous medium and integrating over a volume of tissue, the dissipated power per mass is given by equation (1):

$$\boldsymbol{SAR} = \frac{\boldsymbol{\sigma}|\boldsymbol{E}|^2}{2\boldsymbol{\rho}} \tag{1}$$

Here, σ is the electric conductivity (in S/m), and ρ the mass density (in kg/m^3) and E the scattered electric field (in V/m). This power is dissipated as thermal energy and, hence, increases the temperature in the volume. SAR can increase drastically when the frequency of the RF field approaches or matches the resonance frequency of an implanted device such as an electrode. Resonance can occur when the conductor length matches integer multiples of the half RF wavelength. In MRI, the proton resonance frequency is proportional to the MRI field strength B_0. At $B_0 = 1.5$ T, it corresponds to 64 MHz and the conductor resonance length is $\lambda/2 = 2.43\ m$ when surrounded by free space and $\lambda/2 = 0.27\ m$ when embedded in the later used hydroxyethyl cellulose (HEC) gel with a relative permittivity of $\varepsilon_r = 81$, which is comparable to grey matter with $\varepsilon_r = 74.5$ (Gabriel et al., 1996).

1.4. Evaluation of RF-induced heating in implants

While the origin of the RF heating is well understood, its estimation *in vivo* is still problematic (Erhardt et al., 2018; Nitz et al., 2001), because many parameters influence SAR, especially local SAR at the implant location. Besides the individual anatomy of the patient, additional parameters are of high importance such as B_0, the transmit RF coils and the MR imaging sequence as well as the material, geometry, and, especially, the configuration of the implant (Mattei et al., 2008). For example, the flexible cables of implanted devices can be positioned in many different geometric configurations (Nordbeck et al., 2009), which makes it difficult to predict SAR values for all applicable conditions. Therefore, worst case situations are oftentimes studied where maximum RF heating of an individual implant is created to define conditions for the safe use of the device in MRI. If, in this worst case scenario, the device does not heat up by more than 1 K during 15 min RF exposure, it is considered to be safe under this and less demanding situations. This methodology has been summarized in the international standard ASTM F2182 (ASTM International and West Conshohocken, 2011) and has been employed for ECoG electrodes in MRI (Carmichael et al., 2008). Lately, these time-consuming experimental evaluations have been supplemented widely by preliminary simulations to compute the distribution of electromagnetic fields and SAR hot-spots and then evaluate the worst case, which is ultimately verified in a measurement (Neufeld et al., 2009; Yeramian et al., 2013). These numerical methods have been adopted as “four-tier approach” in the technical specification TS-10974, envisioned to become international standard (ISO, 2012).

1.5. Transport of heat

The incident RF power is absorbed partially by the medium surrounding the electrodes which causes heating of the tissue. The local temperature $T(x,y,z)$ increase results in a temperature gradient ∇T that causes diffusion of heat as described by the heat equation:

$$\boldsymbol{\rho} \cdot \boldsymbol{c_v} \cdot \frac{\partial \boldsymbol{T}}{\partial \boldsymbol{t}} = \nabla \cdot (\boldsymbol{k} \cdot \nabla \boldsymbol{T}) + \boldsymbol{Q_{SAR}} \tag{2}$$

with the density ρ, heat capacity c_v, the thermal conductivity k. The heat Q_{SAR} applied to the system in each voxel is related to the incident RF excitation via (Collins 2004)

$$\boldsymbol{Q}\ \boldsymbol{Q_{SAR}} = \boldsymbol{\rho} \cdot \boldsymbol{SAR}. \tag{3}$$

1.6. Scope of the work

In this work RF heating of planar electrodes is studied during RF exposure in a clinical MRI instrument. In particular, the planar electrode contact diameter's dependency on heating is evaluated. Therefore, local temperatures are measured during MRI with fibre-optic temperature probes (FOTP) in the vicinity of the electrode contacts. Additionally, electromagnetic field simulations are used to assess the local SAR distribution and power dissipation around the different electrode contact diameters, thereby permitting a relative comparison of electrode contact diameters between measurements and between simulation results. Supplementary modelling of FOTPs in the simulations can determine the influence of FOTP on temperature measurements in the direct vicinity of small electrode contacts.

2. Methods

2.1. Samples and experimental setup

Four strips were fabricated (Fig. 1) using established silicone rubber implant manufacturing technology (basic concept described in (Schuettler et al., 2005)). Key features of this technology are a picosecond-laser structured 25 µm Pt/Ir 90/10 foil (Goodfellow GmbH, Hamburg, Germany) sandwiched in medical grade MED1000 silicone rubber (NuSil, NuSil Technology LLC, Carpinteria, USA) with 60 µm layer thickness on the active side of the electrode. Each of the four strips contained four electrode contacts with equal contact size (i.e., exposed electrode contact area due to opening in the surrounding silicone): 4.0 mm; 2.7 mm; 1 mm; 0.3 mm respectively. Single electrode contacts will be addressed in the following as a combination of their position letter and their contact diameter e.g. A40, B27, C10, D03.

Each electrode contact is electrically contacted to a meandering interconnection line (MIL) rendering it stretchable to avoid device failure from strain during and after implantation. The electrode contact pitch is 15 mm, but the MIL length is approximately 17 mm per pitch. The MILs are connected to 34 cm-long PtIr (90/10) wires (75 µm diameter) using resistance welding which amounts to a controlled total lead length variation of approximately 40.8; 39.0; 37.2; 35.4 cm corresponding to the electrode contact positions A-D respectively. The wires are coated individually with a 7 µm polyesterimide layer and all four wires for a strip were encased in silicone rubber tubing of 1.8 mm outer diameter. The cable ends were dip-coated in MED1000 silicone rubber for complete insulation. The strips were placed on a polymethamethylacrylate (PMMA) sample holder where laser marks cut with a CO_2 Versa Laser (Universal Laser Systems GmbH, Vienna, Austria) to ensure reproducible placement of the electrode contacts. Furthermore, a groove in the sample holder ensured identical placement of the implant cable across all strips (Fig. 1).

The entire sample holder was placed into an MRI phantom (Fig. 1) which was adapted from the ASTM 2182–11a standard (ASTM International and West Conshohocken, 2011). Following the standard's instructions, a gelled saline was prepared, meeting criteria for RF heating tests with respect to conductivity, dielectric constant, thermal parameters and the viscosity. The formulation consisted of 29 L distilled water, 31 g/L hydroxyethylcellulose (CAS-No: 9004-62-0, Sigma-Aldrich, St. Louis, Missouri, USA), 1.55 g/L of NaCl, (CAS-No: 7647-14-5, Carl Roth GmbH + Co. KG, Karlsruhe, Germany). The verification of the HEC gel criteria found a conductivity of 0.49 S/m using a conductivity meter (DiST, Hanna Instruments, Germany) and a relative permittivity of 74, measured using a coaxial dielectric measurement kit and a network analyser as described in (Özen, 2013). As these values agreed very closely with the values stated in the ASTM standard, it was assumed, that the viscosity was also high enough to prevent convection. Reproducible sample placement was enabled by a LEGO (LEGO, Billund, Denmark) plate glued to the bottom of the ASTM phantom and consistent placement of the sample holder with very high accuracy.

2.2. Measurement of RF-induced heating

Temperature monitoring was performed using a fibre-optic thermometer (FOTEMP6-19, Optocon AG, Dresden, Germany) that measures the temperature dependent band gap of a GaAs crystal at the fibre tip (Ø 1 mm). It offers 0.1 K resolution at a 1 Hz sampling rate. FOTP were placed orthogonally to the electrode contacts via a second PMMA holder

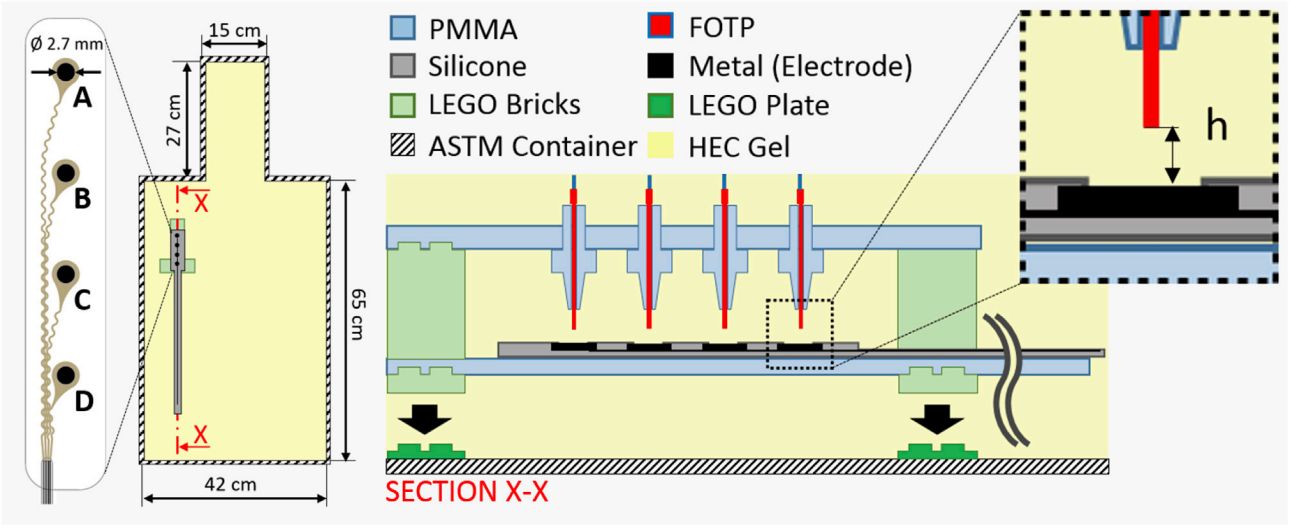

Fig. 1. Strip schematic and the experimental setup. (left) Top view of an exemplary planar electrode "strip" with four electrode contacts of 2.7 mm in diameter (Note that the electrode contact is smaller than the dimension of the whole metal feature) and a cable. The electrode contact centre position on the strips is indicated by letters **A – D.** The four strips are mounted individually on identical, laser cut PMMA holders. These strip holders are plugged into LEGO bricks which allows for reproducible placement in the ASTM phantom. A cross-section (SECTION X-X) along the electrode contacts and the cable axis illustrates the whole experimental setup (not to scale). The FOTPs are fixed by a second PMMA holder that aligns the FOTP in a vertical axis with the electrode contact centre. The distance h between the FOTP tip and the electrode contacts (magnification on the **right**) was varied by replacing all LEGO pieces in one plane by shortened ones. A photograph of this setup is shown in the appendix.

(Fig. 1). The distance of the probe tip to the electrode contact could be varied between 0 and 3 mm by replacing standard LEGO bricks by ones shortened using a milling machine.

Four FOTPs were used to record temperature simultaneously, one for each electrode contact within a strip. The phantom was placed along the edge of the patient table of a 1.5 T MRI system (MAGNETOM Tim Symphony, Siemens Healthcare GmbH, Erlangen, Germany). The FOTP were calibrated in the MRI to avoid a systematic temperature offset caused by the static magnetic field (Buchenberg et al., 2015). The electrode contact position A was placed at the centre of the bore with a lateral offset of 11, 3 cm. A patient weight of 75 kg was assumed, and the energy deposition adjusted by employing a 300 s service sequence with sinc-shaped RF pulses (flip angle of 88° pulse duration of 1 ms) and a repetition time of 50 ms, such that the scanner software indicated a whole body SAR value of 1 W/kg. No gradients were active during the heating experiments.

RF-induced heating was characterized as a relative temperature increase to baseline referred to as ΔT in the following and ΔT_{max} for the maximum temperature increase relative to baseline. The sampling period consisted of a 100 s baseline measurement during inactive MRI sequence, 300 s RF-induced heating, and 200 s cool down. Subsequent measurements were started once the temperature variation had become stable for 1 min within 0.1 K. The measurement of the 4 mm electrode contact strip was repeated 3 times consecutively with a 1 mm FOTP distance to evaluate measurement reproducibility. A background heating measurement in the gel was conducted with the FOTP at the same positions as the previous measurements, but without a strip mounted to the PMMA holder.

2.3. SAR calculation

Initial Temperature slopes, were estimated for each electrode contact from the temperature-time curve $\left(\frac{\Delta T(t)}{\Delta t}\right)$ during the first 10 s of heating (Fig. 2). A 10 s interval was chosen as a compromise between a sufficient number of data points for fitting (sampling rate of 1 Hz), and deviations from the linearity due to heat conduction. Here it is assumed that at the beginning of the heating phase the temperature gradient between the heated region and its immediate surroundings is so small that no heat transfer occurs. From this slope, the SAR values can be calculated as

$$SAR = c_v \cdot \frac{\Delta T}{\Delta t}, \quad (4)$$

where $c_v = 4180 \frac{J}{kg \cdot K}$ is the specific heat capacity of the gel in the phantom.

2.4. Simulations

Finite difference time domain (FDTD) simulations of the E-field and B-field were performed using the software package Sim4Life (Version 3.4, ZMT AG, Zurich, Switzerland) to investigate the pointwise SAR distribution in the simulation lattice and local 1 g SAR around the excited electrode contacts. Fig. 3 shows the setup and the simulation environment. The elongated implant cable is the main cause of heating at the electrode contacts which is very time-consuming to simulate, therefore the cable was replaced in the simulation by a harmonic voltage edge source ($f = 64$ MHz, power: $P = 85\ \mu W$) at the transition of the cable to the MIL. For each diameter only one electrode contact per strip was simulated, and the electrode contact was assumed to be a perfect electric conductor and with identical MILs to ensure comparability between simulations (Fig. 3). The metal electrode disc was covered by a 60 µm isolating silicone layer ($\varepsilon_r = 3, \sigma = 0\ S/m$) except for the contact, and a surrounding $10 \times 10 \times 17$ cm^3 volume of HEC gel ($\varepsilon_r = 81$, $\sigma = 0.47\ S/m$) was modelled as in the measurements. The smallest voxel size was 0.04 mm^3 and the calculation time was between 15 and 20 h, depending on the electrode contact size (using GPU acceleration, one

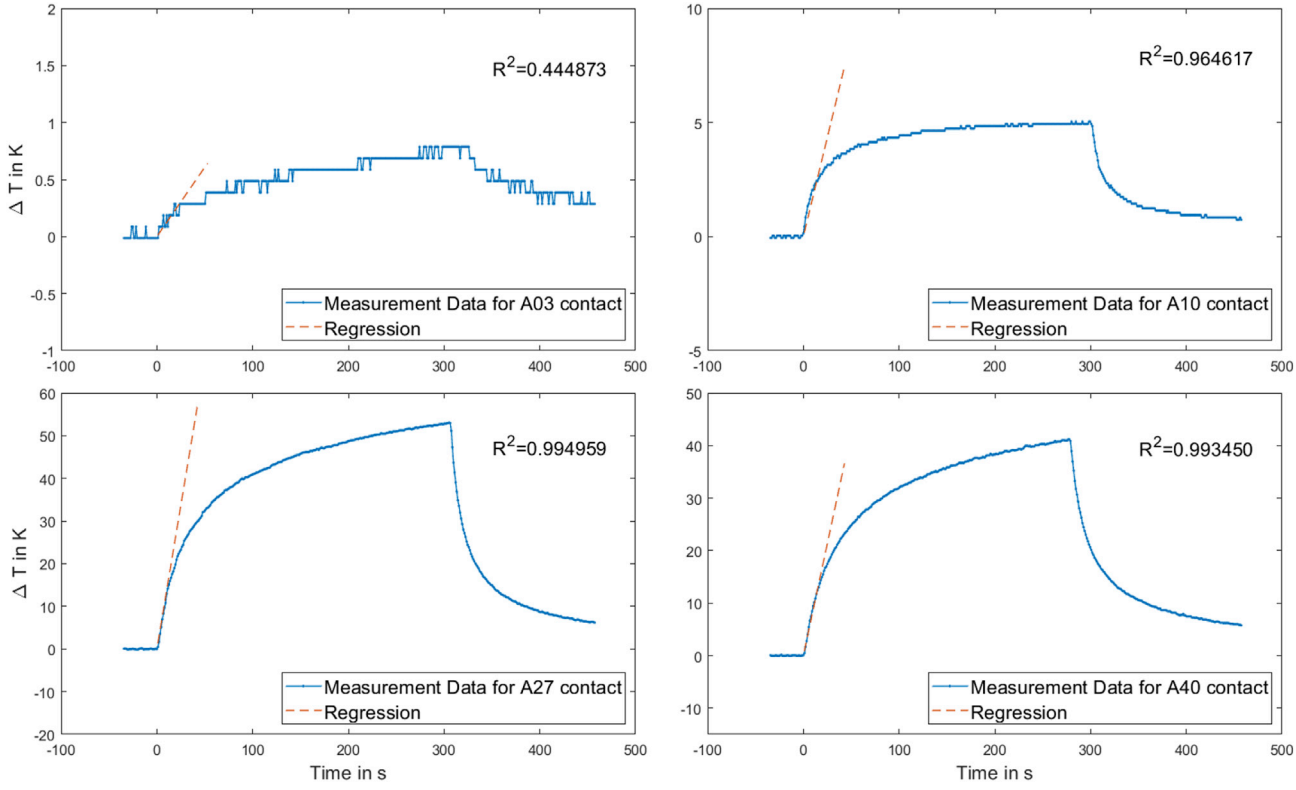

Fig. 2. Recording of the ΔT of A03. A10, A27 and A40 with a FOTP in contact with the electrode contact over a 5 min RF heating period. The preceding 100 s measurements (t < 0) serve as baseline for the displayed ΔT and are shown only partially. The cool down period starts at ~300s. The resulting regression and R^2 values are shown. Note the changing y-axis scaling of the plots.

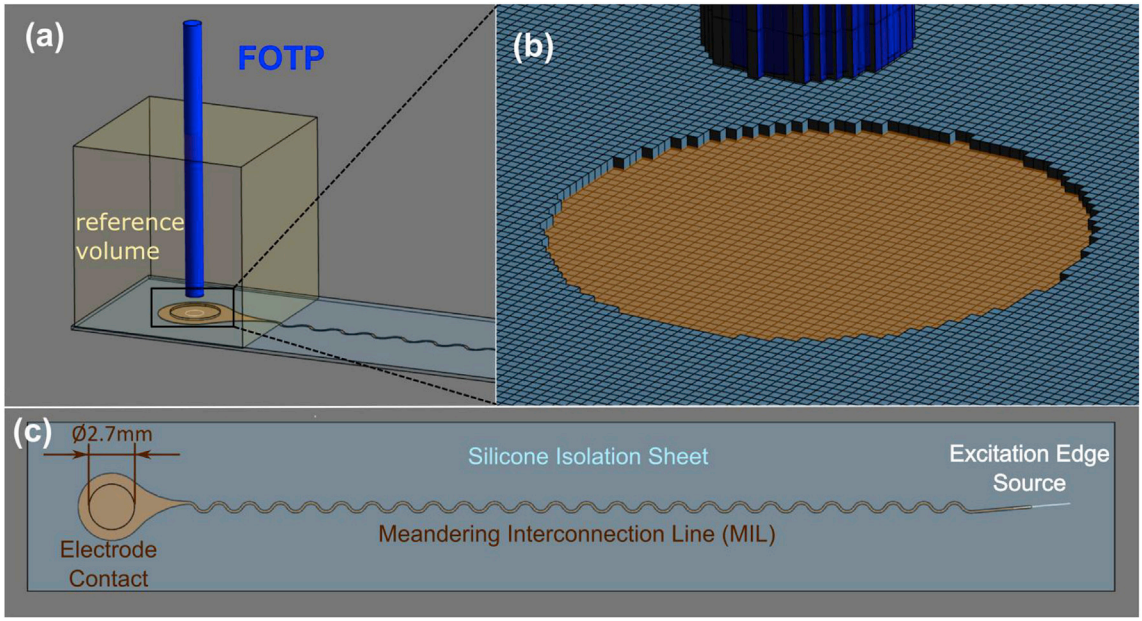

Fig. 3. Simulation setup: (a) The electrode strip with the $1 \times 1 \times 1$ cm^3 reference volume used for integration of SAR to receive local 1 g SAR. The blue cylinder is modelled with glass material properties to mimic the FOTP. **(b)** The simulated mesh grid zoomed in on the 2.7 mm contact site with the FOTP in 1 mm distance. **(c)** Whole simulation setup with electrode contact, MIL, silicone isolation and the excitation edge source mimicking the RF induced power.

GeForce Tesla C2075). Maximum pointwise SAR values were derived voxelwise from the resulting electromagnetic fields.

FOTPs were implemented as glass cylinders ($\varepsilon_r = 4.82, \sigma = 0.0043$ S/m). Simulations were performed with and without the FOTPs to investigate systematic errors caused by the presence of relatively large FOTPs. Two different FOTP placements were tested: direct contact or 1 mm above the electrode contact. Mean SAR above the electrode contact was calculated via integration over a $1 \times 1 \times 1$ cm^3 reference volume centred on the electrode contact resembling 1 g of "tissue".

2.5. Temperature simulations

The simulated SAR distributions were used to calculate temperature distributions $T(x, y, z, t)$. Therefore a discretized version of the heat equation (Collins et al., 2004) was implemented in Matlab (Simulation data and Matlab code is available upon direct request). A volume of $1.6 \times 1.6 \times 1.6$ cm^3 centred above the contact site was chosen for the simulation domain. The HEC gel was modelled with the parameters $k = 0.62$ (W/m/K) $\rho = 993\ kg/m^3$ and $c_v = 4180 J/kg/K$ (ISO, 2012), and an absorbing boundary condition was implemented. Furthermore, it was assumed that the FOTP integrates the temperature over a cylinder of 1.5 mm length and a radius of 2 mm diameter centred to the temperature sensor position.

Heat pulses Q_{SAR} were applied to the simulation volume using the simulated SAR distribution. The heat equation (2) was then used to iteratively calculate the heat distribution at time steps of $\Delta t = 0,005\ s$ (i.e., at 10 steps per TR) before the next heat pulse was executed. A temperature-time curve was extracted for the 2.7 mm electrode contact which was compared to the FOTP measurement. The simulation input power level (magnitude of heat pulse) was varied until the temperature difference between measurement and simulation was minimal at the end of the heating period. This power level was subsequently applied in the simulations of the other three electrode contact diameters.

3. Results

3.1. Temperature measurements

A steady temperature increase of up to 1.3 K/s was seen during RF excitation in all experiments. A characteristic temperature-time curve and the initial temperature slope is shown in Fig. 2. Over the RF excitation period of 5 min ΔT_{max} of up to 53 K were observed, ΔT_{max} for each FOTP distance, contact diameter and electrode contact position is shown in Table 1 and the entire set of corresponding temperature-time curves are displayed in Appendix 1. For each individual measurement ΔT_{max} at position A is at least 19% higher than at any other position – except for the measurement where the FOTP is in contact with the 0.3 mm electrode contact. Normalized to the temperature of the 2.7 mm contact for each

Table 1
Maximum temperature difference $\mathbf{\Delta T_{max}}$ in K for each FOTP distance (contact - 3 mm), contact diameter, and electrode contact position A-D. The largest ΔT_{max} was found for the A27 with the FOTP in contact. Comparing the ΔT_{max} within the same FOTP configuration a clear decrease with decreasing MIL length (drop from position A towards D) is visible expect for the 0.3 mm electrode contact with the FOTP in contact. Increasing FOTP distance from the electrode contact shows decreasing ΔT_{max} except for the 0.3 and 1 mm electrode contact in contact with the FOTP.

Contact Ø in mm	0.3 (ΔT_{max} *in K*)	1.0 (ΔT_{max} *in K*)	2.7 (ΔT_{max} *in K*)	4.0 (ΔT_{max} *in K*)
Electrode contact position:	*FOTP in contact with electrode contacts*			
A	0,79	5.04	53.08	41.16
B	1.10	5.30	34.52	25.30
C	1.75	3.58	23.59	17.38
D	2.40	4.10	19.00	13.80
	FOTP in 1 mm distance of electrode contacts			
A	3.71	10.19	29.10	27.03
B	2.90	6.80	21.20	19.38
C	2.35	4.79	14.94	13.24
D	2.20	3.70	11.10	10.55
	FOTP in 2 mm distance of electrode contacts			
A	2.63	6.91	23.60	21.52
B	2.32	4.68	17.90	15.91
C	2.03	3.64	12.90	10.90
D	1.80	2.90	10.00	8.45
	FOTP in 3 mm distance of electrode contacts			
A	2.06	4.90	16.74	17.90
B	1.90	3.60	13.08	13.30
C	1.68	2.68	9.49	9.09
D	1.50	2.23	7.04	6.90

FOTP distance, a mean relative standard deviation of 0.14 was found for ΔT_{max} at the positions A-D. Hence the electrode contacts at different positions show comparable behaviour and while the following discussion focuses on position A, it holds valid for all other position.

The three consecutive repetitions of the 4 mm contact strip had an absolute standard deviation of 1.5, 1.3, 1.3, 1.9 K for the electrode contact positions A-D which leads to a mean relative standard deviation of 0.06. The background temperature measurements without the electrode strip, but with the FOTPs in 1 mm distance configuration showed a ΔT_{max} below 1 K at all four sensors (Appendix 2).

Fig. 4a shows ΔT_{max} at all position A electrode contacts. The ΔT_{max} decreases with FOTP distance except for two locations where the FOTPs were in contact with A03 and A10. Fig. 4a also shows that the highest ΔT_{max} is observed for A27 independent of the FOTP distance, followed by A40, and then the electrode contacts with the two smallest diameters.

The initial temperature slopes were calculated by linear regression of the measured temperature-time curves and are shown in Fig. 4b. The regressions' lowest $R2 = 0.44$ was seen for the contact measurement of A03 (median $R^2 = 0.96$, IQR $(R^2) = 0.07$)). The highest slope was seen for A27 in contact with a FOTP. When the FOTP was not in contact with the electrode contact, derived temperature slope values decreased with increasing FOTP distance.

3.2. Simulations

Fig. 5 shows the results of the FDTD simulations around the electrode contacts. Although all electrode contacts were excited with the same input signal, the resulting pointwise SAR is distributed over a volume that scales with the diameter of the electrode contact, but the depth, up to which significant pointwise SAR is found, is largest for contact diameter 2.7 mm. The 2.7 mm and 4 mm contact show a dip in SAR intensity above the centre of the electrode contact. Table 2 lists the maximum pointwise SAR values and the local 1 g SAR in the reference volume above the electrode contact. The maximum pointwise SAR increases with decreasing diameter and shows a 92-fold higher SAR at the 0.3 mm contact compared to the 4 mm contact. The mean SAR in the tissue increases with the electrode contact diameter: from a diameter of 0.3 mm–2.7 mm the SAR increases by a factor of almost four, while the energy deposition at the 2.7 mm is 34% larger than at the 4 mm electrode contact.

Summarized in Table 3 are the simulation results with a FOTP that is either directly in contact with the electrode contact or placed 1 mm above the electrode contact surface. At a 1 mm distance the local maximum and mean SAR is almost identical compared to the values

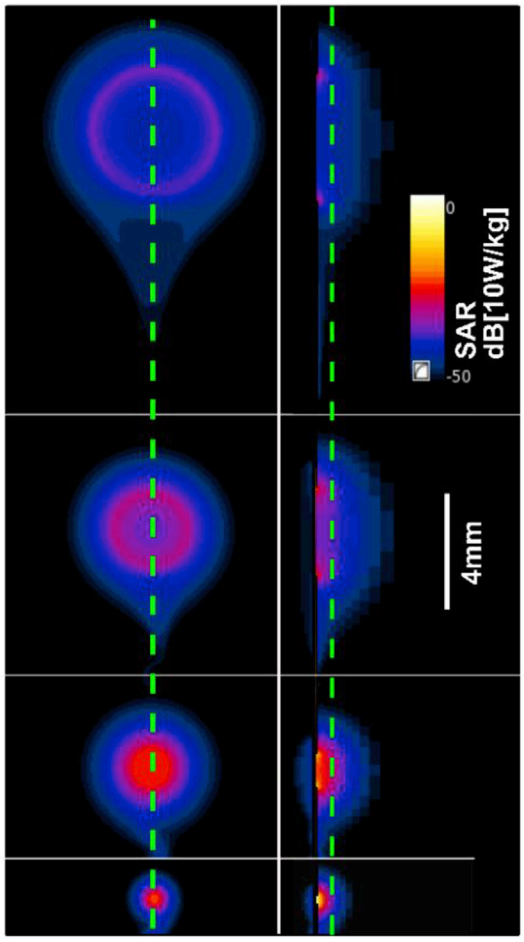

Fig. 5. SAR maps for each electrode contact in frontal and lateral views. The frontal view (left) displays pointwise SAR values in a parallel plane 0.8 mm above the electrode contacts (dashed line in right panels) in the range of 0 to −50 dB where 0 dB corresponds to 10 W/kg. With increasing electrode contact diameter the SAR is distributed over an increasing area while the intensity is decreasing. The lateral view (right) shows SAR values perpendicular to the electrode contact plane along the central axis (dashed line in left panels) using the same scale. The difference in the SAR distribution into the tissue adjacent to the different electrode contact diameters becomes evident.

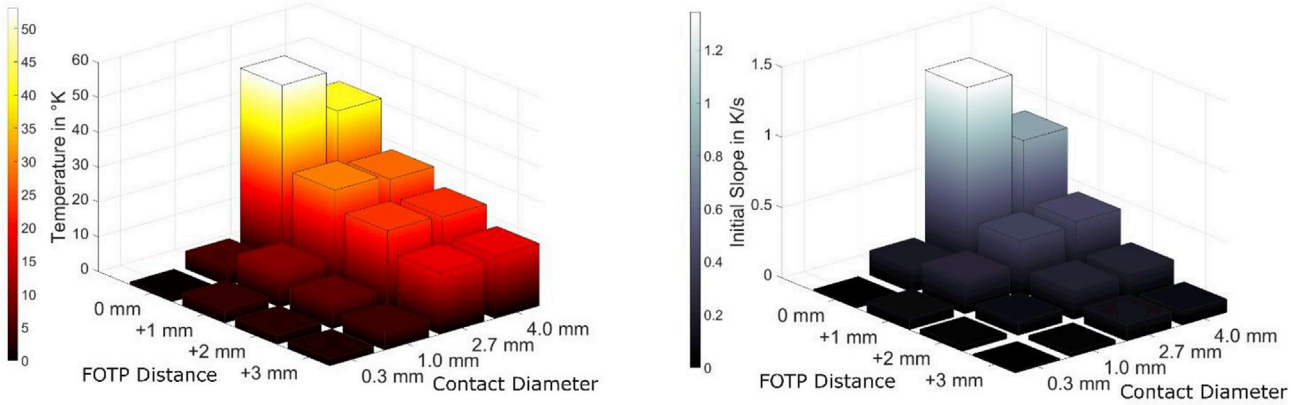

Fig. 4. a (left): Overview of ΔT_{max} measured at A40, A27, A10 and A03 as a function of the 0–3 mm distances between electrode contacts and the FOTPs. **b (right):** Overview of the initial temperature increase in K/s derived from the slope of the ΔT measurements. The similar relative distribution is noticeable and due to the same data origin, nevertheless, the close relation between measured temperature and SAR becomes visible.

Table 2
Maximum pointwise SAR and local 1 g SAR in both the reference volume calculated from the simulated E-field data. While the local SAR decreases with contact diameter, the mean SAR maximum is found at 2.7 mm, which is in agreement with the measured data.

Contact Ø in mm	pointwise SAR Max in W/kg	local 1g SAR in pW/kg
0.3	2.218	0.0181
1.0	0.451	0.0527
2.7	0.077	0.0649
4.0	0.024	0.0482

Table 3
Maximum pointwise SAR and local 1 g SAR in the reference volume calculated from the simulated E-field data in the presence of a modelled FOTP placed in contact and in 1 mm distance configuration relative to the electrode contact centres. While the FOTP introduction shows only a small reduction of the local 1 g SAR for the 4.0 mm and the 2.7 mm electrode contacts in contact configuration compared to the absent FOTP data of Table 2, a significant reduction of 89% and 87% in local 1 g SAR respectively was found for the 1 mm and 0.3 mm electrode contacts.

FOTP distance	1 mm	1 mm	In contact
Contact Ø in mm	Pointwise SAR Max in W/kg	Local 1g SAR in pW/kg	Local 1g SAR in pW/kg
0.3	2.201	0.0180	0.0023
1.0	0.443	0.0521	0.0054
2.7	0.077	0.0644	0.0637
4.0	0.024	0.0480	0.0479

Table 4
Simulated maximum temperature $\mathbf{T_{max}}$ in K obtained by integration volume around FOTP for previous distances (contact - 3 mm) and all four contact diameters.

Contact Ø in mm	0.3 (ΔT_{max} *in K)*	1.0 (ΔT_{max} *in K)*	2.7 (ΔT_{max} *in K)*	4.0 (ΔT_{max} *in K)*
FOTP distance	Temperature Simulation			
Contact	19.42	79.32	57.66	27.01
1 mm	7.08	36.47	47.71	29.09
2 mm	3.65	19.69	32.85	23.58
3 mm	2.20	11.92	22.49	17.81

without a FOTP. Placing the FOTP in contact with the electrode contact reduced the mean SAR by 87% for the 0.3 mm and by 90% for the 1.0 mm electrode contact (compared to no FOTP present), whereas the larger electrode contacts were unaffected.

The simulated temperature values in Table 4 were obtained from the integration volume of the FOTP. They correspond to the contact position A in the data of Table 1. The largest ΔT_{max} of 79 K was found at 1 mm with the FOTP in contact. For electrode contact diameters of 0.3–2.7 mm, the temperature decreased with increasing distance, and for the 4 mm-electrode contact diameter the maximum temperature is observed not directly at the surface, but at 1 mm distance. The comparison between simulation and measurement for 2 mm and 3 mm distances shows a mean error of 6.83 K, where the 2.7 mm electrode contact shows the largest deviation of 18.2 K at 2 mm spacing. Overall the largest deviations are 96% and 94%, for the contact measurement of the 0.3 mm and 1 mm electrode contacts, respectively. An exemplary temperature map of a 2.7 mm electrode contact and temperature time-curves for all electrodes can be found in Appendix 5.

4. Discussion

The exposure of implanted electrodes to the RF field in MRI can focus the E-field in adjacent tissue, which can cause an increase in SAR with subsequent tissue damage (Erhardt et al., 2018; Nyenhuis et al., 2005). Therefore, preventing RF-induced heating beyond acceptable limits is important because patients with implants often need to undergo MRI exams after electrode implantation but MRI may also get indicated for implant unrelated reasons. Due to the many parameters that influence heating and the lack of complete analytical formulation, RF-induced device heating is typically evaluated by temperature measurements in gel phantoms to assess MRI safety of individual implants. One central geometric parameter is the electrode contact diameter. In this work the influence of the electrode contact diameter on RF-induced tissue heating was studied using both established temperature measurement techniques as well as with field simulations.

4.1. Temperature measurements

The measurements with the FOTP showed that the electrode contacts with the longest MILs (position A) yield the highest ΔT_{max} (at least 19% larger) during RF exposure compared to identical electrode contacts with shorter MILs. Higher ΔT_{max} values are expected, as an increase of the conductor length towards the wavelength results in an increased RF absorption by the antenna formed by the lead, and, thus, to a higher RF energy coupled to the electrode contact.

The observed increase of ΔT_{max} for FOTP closer to the electrode contacts is also expected, as the energy deposition should be the highest at the interface between electrode contact and gel. At very low electrode contact diameters of 0.3 mm and 1 mm, however, the measured ΔT_{max} is notably decreased. As the temperature probes have a diameter of 1 mm, they lead to a removal of the gel in the vicinity of the electrode contact, which in turn causes a lower energy deposition. This systematic effect needs to be considered when electrode contacts are investigated whose dimensions are similar to the FOTPs and might also account for the poor performance of the regression of the initial slope calculation.

It is interesting to note that ΔT_{max} of the 4 mm electrode contacts is lower than the 2.7 mm electrode contacts, which can be explained by a larger volume in which the power is dissipated. This relationship between the input energy and the distribution volume is also seen in the simulation results (cf. Table 2). In clinical practice patients with implanted electrodes will undergo MRI exams after surgery, and the choice of the optimal electrode contact diameter should thus also take into account the tolerable amount of local heating in the vicinity of the electrode contacts. To better asses the expected tissue damage, the use of a tissue damage model like CEM43 (van Rhoon et al., 2013) could be applied.

4.2. Temperature measurement method

The fibre-optic temperature measurement method used in this study is recommended by the US food and drug administration (FDA) for the evaluation of MRI compatibility of implantable devices, and it has been used for similar testing of elongated implants leading to FDA certification (Shellock, 2007). However, especially at small electrode contact diameters (0.3 mm and 1 mm) the presence and positioning of the FOTP strongly influenced the measurement result. As discussed above, the displacement of the tissue-mimicking gel by the sensors changes the local RF heating properties, and results in an underestimation of heating. In the simulation this systematic error can be studied – here, a glass cylinder with electromagnetic properties similar to the FOTPs was introduced. The simulations showed that in the absence of the FOTPs much higher SAR values can occur. To reduce this systematic error, smaller FOTPs should be used, however, no FOTPs with diameters smaller than micro-electrode contacts are commercially available.

In this work an orthogonal placement of the four FOTPs to the electrode contact surface was chosen. While Mattei and co-workers suggest a

transverse configuration for pacemaker leads (Mattei et al., 2007) our results indicate that an orthogonal configuration is more reproducible, because the distance of the active temperature sensor to the tip is varying by only ±0.5 mm (according to manufacturer specifications). At an orthogonal placement the active temperature sensor is always located in the centre of the electrode contact, whereas a lateral position error of up to 1 mm would lead to significant temperature deviations in particular for the small 0.3 mm electrode contacts.

As an alternative to invasive temperature probes, MRI thermometry could be used to image the heat dissipation (Ehses et al., 2008), which would be beneficial compared to a temperature measurement at a single point as provided by FOTPs. Additionally, systematic errors from gel displacement would be avoided by the non-invasive MRI technique. However, MR thermometry is hampered by susceptibility artefacts which can be especially pronounced near implants. MRI thermometry has a temperature resolution of about 1 K (Quesson et al., 2000), which might be challenging for small ΔT_{max} as found near the smaller electrode contacts. Another limitation of MRI thermometry is the spatial resolution: at 1,5 T an imaging resolution of about one millimeter can be achieved in dynamic MRI thermometry, which might not be sufficient for small electrode contacts.

The interactions for a particular electrode configuration with the MRI system are dependent on many parameters such as scanner, transmit B1 coil, field strength (Neufeld et al., 2009; Thornton, 2017). These variations mostly affect the magnitude of the heating observed at the implant. For the relative influence of the electrode contact diameters studied in this work the linear dimensions and the precise E-field distribution along the antenna formed by the MILs need to be considered. The effect of this coupling antenna can be described by a transfer function approach [Park 2007] so that the energy input via the antenna can be separated from the energy deposition near the electrode contacts. This justifies the use of a voltage source in the simulations instead of a full simulation including the cables which would be very time-consuming – the high-resolution simulations in the vicinity of the electrode contacts alone required computation times of several days.

The measurement setup in this study was chosen to induce high temperature changes - the connecting cables were fully immersed inside the gel and they were placed close to the rungs of the birdcage body coil where high electric field strengths are present (Nordbeck et al., 2008) to operate in a regime, where significant heating is observed. The cable length of the strips was in a length range where resonant heating was expected - a length, which is commonly used in clinical practice. The phantom gel was so viscous that convective cooling could not affect the temperature distribution (Park et al., 2003). Nevertheless, during the heating measurements the RF power deposition of 1 W/kg calculated by the MRI system remained far below the regulatory limits of 4 W/kg whole body SAR as effective in the US. Still ΔT_{max} of up to 53 K was measured near the electrode contacts, which might be dangerous for patients with implanted electrodes. (The power deposition had been adjusted as the phantom gel had started to cook in preliminary experiments using 2 W/kg). In ASTM temperature measurements data is acquired over a 15 min period – here, the RF exposure was shortened to 5 min, as the most heating occurs in this time span. Additional measures must be taken to extrapolate from these findings to other electrode contact diameters or even other geometries. To safely use the tested electrodes in a clinical setting a safety index (Yeung et al., 2002) approach could be used where the transmit RF power is lowered by a pre-defined factor, so that the ΔT_{max} in the vicinity of the electrode contacts stays below 1 K. In the presented setting – neglecting any heat transport (e.g. perfusion) but conduction, this index might be as high as 1344, which means, that for example the flip angles in the MR sequences need to be reduced by $\sqrt{1344} = 36.6$, a factor, that would likely be impractical.

4.3. Effect of cable end configuration

Another factor influencing the RF-induced heating of the electrode contacts is the electric termination of the connecting cables (Özen et al., 2019). In this study the cable ends were insulated, as the manufacturer recommends to avoid short-circuited cables because cable loops may pose a safety hazard (Dempsey et al., 2001). The potential of an insulated cable end is more reproducibly defined than that of an open-ended cable – nevertheless, a floating cable configuration was also tested in preliminary measurements, and an approximately threefold lower ΔT_{max} was found. This finding is in agreement with precedent studies on pacemaker leads. It was shown that higher ΔT_{max} for insulated cable terminations occurred than for the gel exposed configuration (Langman et al., 2011). These results emphasize that implant manufacturers need to carefully assess the effect of termination impedance on device safety.

4.4. Simulations

To assess the relative difference in heating with respect to the electrode contact diameter, as many influencing factors as possible were removed from the simulation. Thus, the electrodes were simulated with single electrode contacts. The results of the FDTD simulations (Table 2) suggest that a significantly larger volume is heated in the vicinity of the larger electrode contacts while the pointwise SAR is reduced, whereas SAR is locally concentrated and increased for the smaller electrode contacts. The total deposited power is three times higher for the three larger diameters than for the smallest. For each clinical application it is therefore necessary to decide whether a large electrode contact diameter with an associated higher energy deposition over a larger area is preferable over a smaller electrode contact with a reduced energy deposition but a 92-fold higher energy density in a small volume. In recent years, this focussing effect has led to the quantification of SAR values in larger (10 g tissue) and smaller (1 g tissue) volumes (Wang et al., 2007). The simulation results presented here suggest that for implanted electrodes most of the energy deposition occurs in a volume equivalent to 1 g tissue, and that this value or even less should be used for safety assessment.

Simulations with an FOTP probe confirm that lower temperatures are detected in the presence of the FOTP sensor due to gel displacement (Table 3). While the presence of the FOTP at a distance of 1 mm from the electrode contact did not change the mean SAR, a systematic error was found when the FOTP was in contact with the electrode contact. This error was highest for smaller electrode contact diameters. This again emphasizes the need for a less invasive temperature measurement method.

At the 4 mm electrode contact a lower maximum temperature was found compared to the 2.7 mm electrode contact, which is well in line with the simulations, but the 1 mm electrode contact has higher mean SAR than the 4 mm electrode contact, which is not reproduced in the measurements.

The ring-like SAR distribution along the electrode contact edge (cf. Fig. 5), compared to the more peaked distribution at the 1 mm and 0.3 mm electrode contact, makes the smaller electrode contacts even more susceptible to systematic positioning errors, which might explain the discrepancy between 1 mm electrode contact in simulation and measurement. In the field of electrical stimulation, it is a well-known phenomenon that the current density is highest at the edge of an electrode contact and close to zero in the centre. This effect becomes more distinct with increasing frequency as has been observed in the typical frequency range for electrical stimulation of low kHz (Behrend et al., 2008) and decreases with the aspect ratio of the electrode contact diameter to silicone edge (Rubinstein et al., 1987; Suesserman et al., 1991) - a phenomenon that may also occur at the MHz frequencies used

in MRI. This effect could be investigated by a spatially resolving measurement method such as MRI thermometry or the direct measurement of the electric fields distribution (Reiss et al., 2015), which would have the added benefit of no heat conduction.

The integration of the simulated temperatures over the volume of the FOTP sensor yielded temperature values which had the same ordering as the measurements with the FOTP, i.e. a maximum temperature for 2.7 mm electrode contact diameter. The absolute temperature values, however, differ by up to a factor of 2.9 between simulation and measurement. Here, the values the FOTP in contact and 1 mm distance were not considered which can be justified by the gel displacement of the FOTP that severely influences the heating.

The simulated temperature-time curves show a steeper increase than the measurements which suggests that an additional heat sink is present during the experiment. The simulation does not take into account the heat conduction of the electrodes which could remove heat from the system. Additionally, convective heat transport in the gel cannot be totally excluded. Nevertheless, the measurements and simulations agree within a factor of 1.6 for the largest electrode diameters (2.7 mm and 4 mm) that are less affected by the presence of the FOTP. The comparison of the measured and simulated temperature-time curves for all electrode contact diameters at 2 mm FOTP distance (cf. Appendix 5) shows the same ordering for maximum temperature values.

4.5. Comparison of the findings with previous studies

Only a few publications analyse the safety aspects of MRI exams in patients with implanted electrodes (Hawsawi et al., 2017). In this phantom study, the maximum ΔT_{max} of 53 K was significantly higher than that reported in previous studies with similar kinds of implant by Carmichael et al. (6.7 K) (Carmichael et al., 2008), Carmichael et al. (6.9 K) (Carmichael et al., 2010), Boucousis et al. (10 K) (Boucousis et al., 2012), Ciumas et al. (0.9 K) (Ciumas et al., 2014), Ahmadi et al. (10.1 K) (Ahmadi et al., 2016) and Bhattacharyya (12 K) (Bhattacharyya and Klapperich, 2007). Comparison of the temperature changes is difficult as the MRI field strength, the implant configuration, implant construction, the imaging object, imaging sequence parameters, and applied SAR are not consistent between all these studies. Here, the implant was placed fully immersed, with a straight cable in the coronal plane of the right arm region within the ASTM phantom where the highest z-component E-field is expected (Nordbeck et al., 2008). Contrarily, all the previous studies placed the implants more centrally in the head region to mimic the clinical configuration, where major parts of the cables and the cable end were surrounded by air. Reducing the immersed length of the conductor changes the RF resonance length, and the central position of the cables leads to a lower E-field exposure. Thus, our study more closely mimics a scenario, where the patient is placing the head more laterally.

Yang et al. recently reported that in over one thousand patients with subdural stainless steel electrode contacts with 4 mm diameter who have been imaged with MRI no adverse outcomes related to MRI have been observed (Yang et al., 2012). Even though this result shows that the situation studied here is not encountered in clinical settings, a notable uncertainty remains as to the possible heating effects that can occur. Despite the magnitude (quantity) of the heating is strongly influence by the extent the cables are immersed (implanted) and the location of the device itself relative to the MR scanner, the qualitative relationship between contact diameter and MR induced heating stays valid: Reducing the electrode contact diameter may help to reduce the total amount of energy dissipated into the electrode vicinity, but increases the pointwise SAR at the contact.

4.6. Applicability of findings to electrodes used for different applications

Implantable electrodes used for different applications such as DBS or depth electrodes have not been investigated. The shape of these electrodes significantly differs from the geometry investigated here, and thus the influence of the electrode contact size on the heating properties cannot be derived from the presented findings. Recent studies suggested DBS electrodes with planar electrode contact diameters of 50 µm (Vajari et al., 2018), and changing electrode contact sizes and present FOTPs may still influence the heating pattern.

5. Conclusion

Heating measurements for a range of planar electrode contact diameters showed a maximum temperature increase between 0.8 K and 53 K in a MRI system during a 5 min RF power deposition of 1 W/kg. Heating measurements close to electrode contacts with a diameter equivalent or smaller than the temperature sensor, where they seem to be needed the most, are compounded by gel displacement. Comparing simulations of 0.3 mm–4 mm electrode contacts showed 92-fold higher pointwise energy density, but one third of the total energy dissipation. Accordingly, the diameter of planar electrode contacts has a strong influence on the local distribution and the total amount of dissipated RF-induced heating around the electrode contact. Small electrode contacts may thus be more prone to exceed safe tissue temperature thresholds, while being more likely to stay within regulatory safety limits that average over a volume.

Acknowledgements

The authors thank Miguel Ulloa for design and production of the strips. The work presented here was financially supported by the BrainLinks-BrainTools Cluster of Excellence funded by the German Research Foundation (DFG, grant number EXC 1086) and by the National Institutes of Health (R21 HL127433) to DBE.

Appendix

Appendix 1: The background shows the LEGO sample holder (compare to Fig. 1) with the FOTPs in contact configuration (red) with the 0.3 mm electrode contacts. The blue glass fibres were fasted by plastic screws throughout entire experiments. The three other sample holders with the three larger electrode contact diameters are shown in the foreground. The cables are embedded in a groove along the PMMA holder to guarantee a reproducible cable configuration in the phantom (not shown).

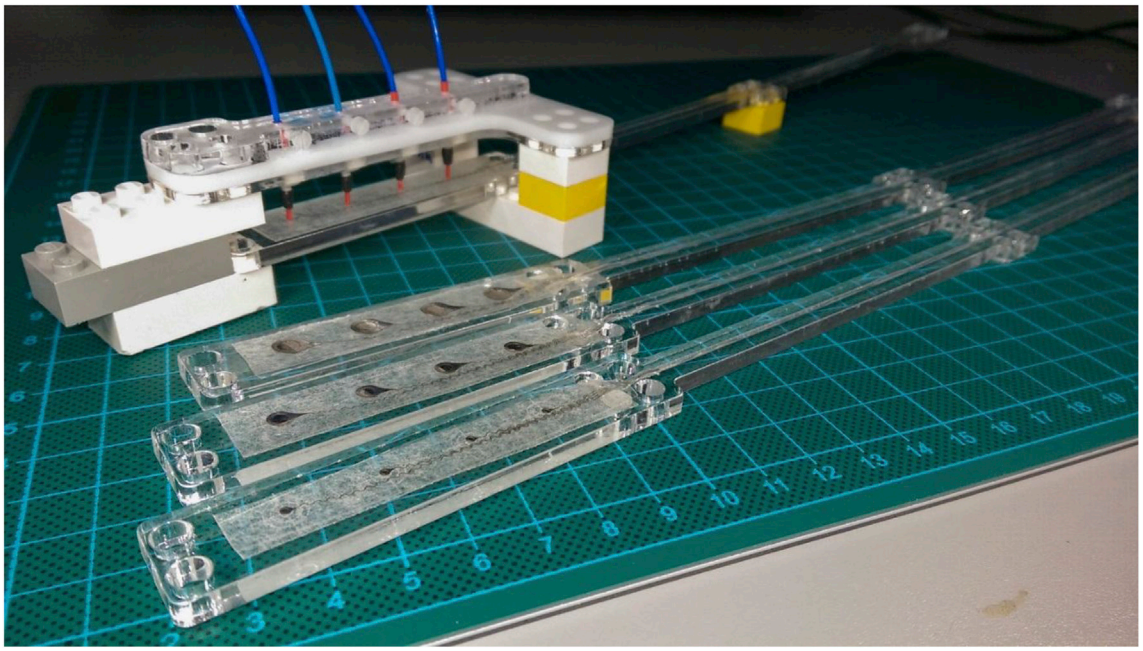

Appendix 2: Phantom container adapted from the ASTM 2182-2011a testing method filled with HEC gel during preliminary investigations. The green object in the gel resembles a LEGO plate glued to the containers floor. The blue cables represent the glass fibres of the FOTPs.

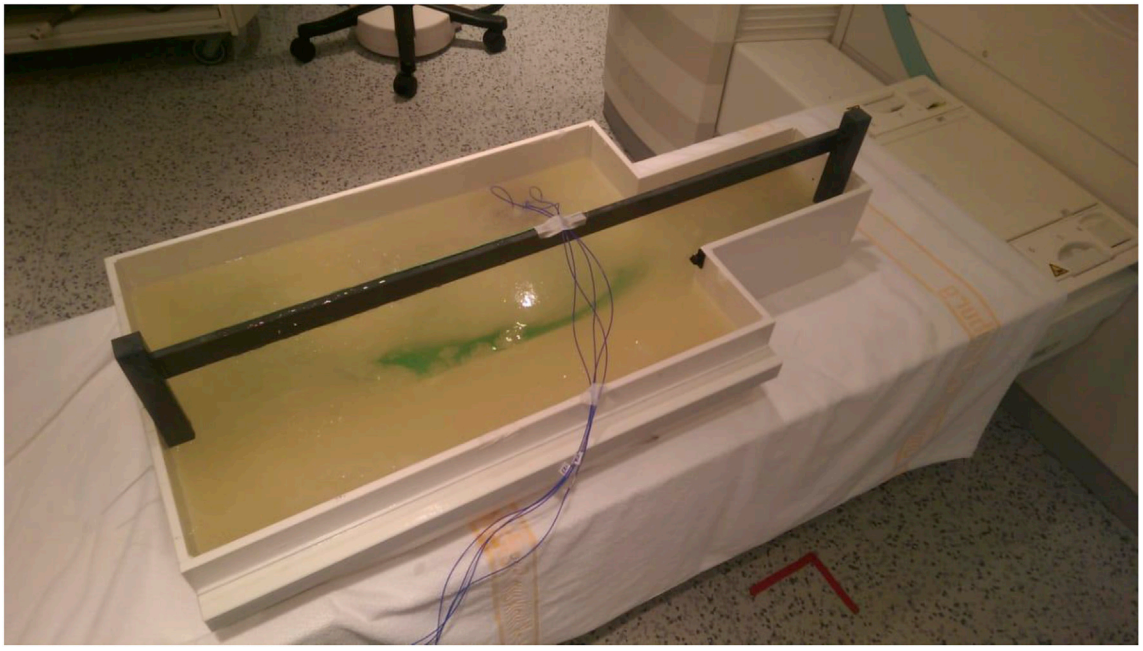

Appendix 3: All acquired temperature-time curves with varying contact diameter, FOTP distance and electrode position.

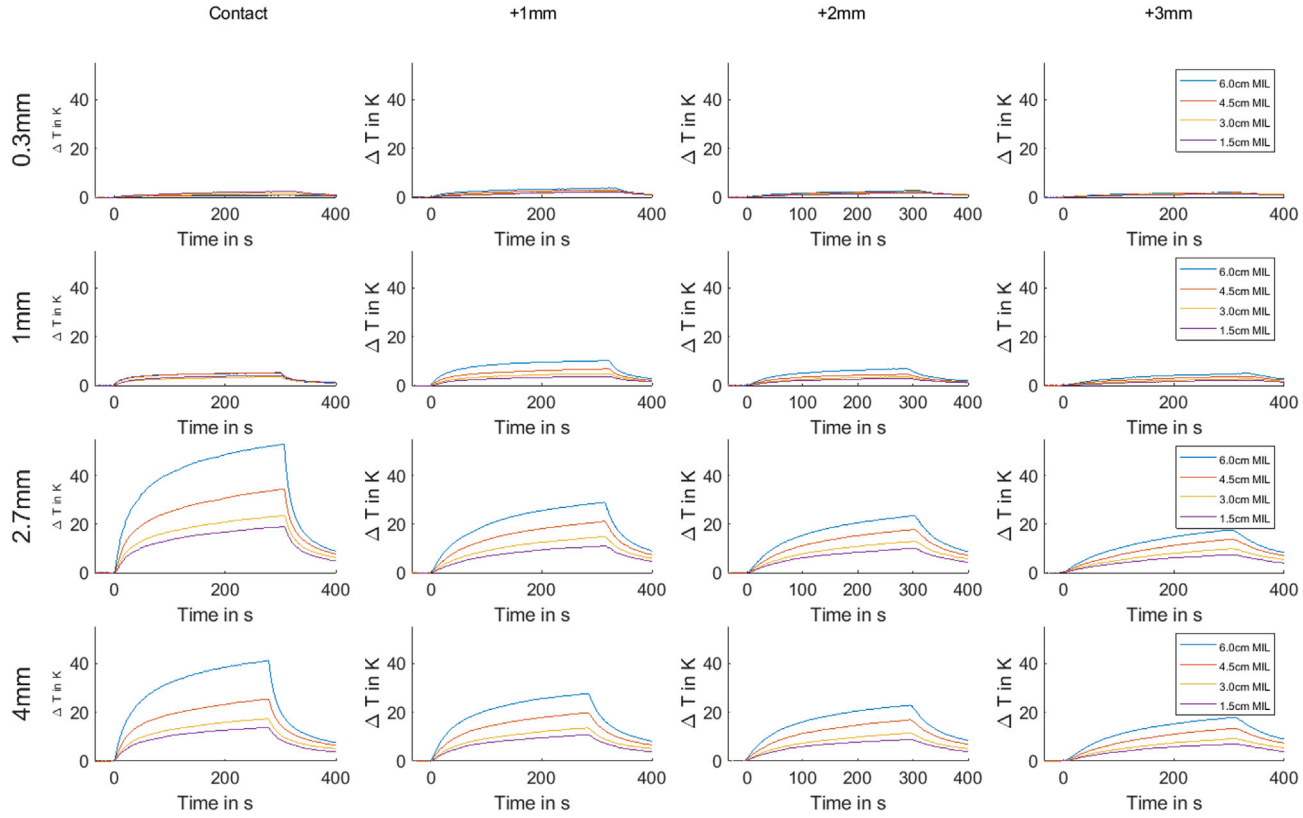

Appendix 4: Background measurement with FOTP in +1 mm distance configuration and absent electrode strip.

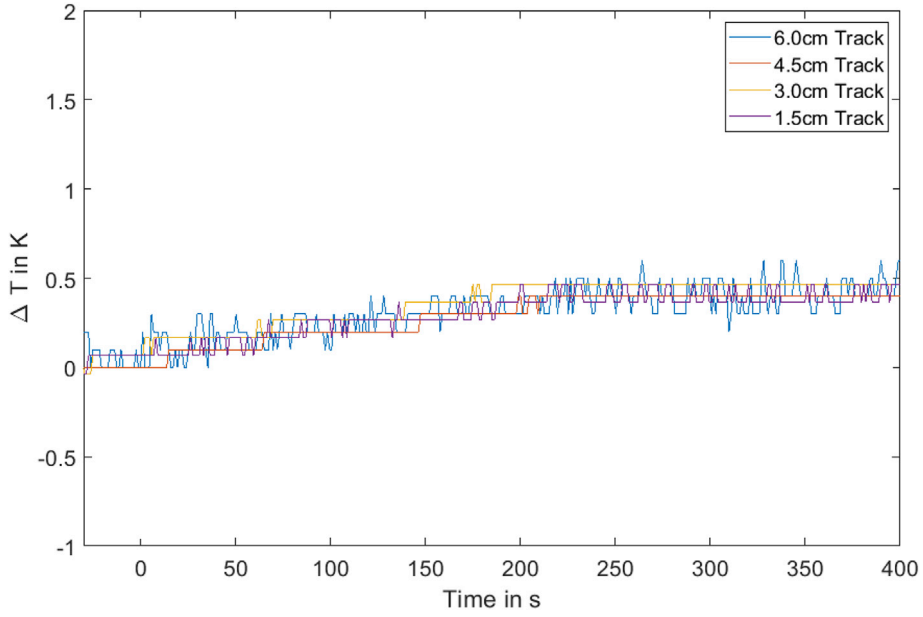

Appendix 5 (Left): Cross sectional temperature distribution simulated at the 2.7 mm electrode contact diameter (after the last heating pulse was applied). White line at the lower end indicates the electrode contact site **(Right):** Compilation of measured and simulated temperature-time curves for various electrode contact diameters with the FOTP in 2 mm distance of the electrode contact. The input power was chosen such that the maximum temperature increase at the 2.7 mm electrodes agree between measurement and simulation. The simulated curves increase more rapidly which might be attributed to a presence of an additional heat sink in the measurement.

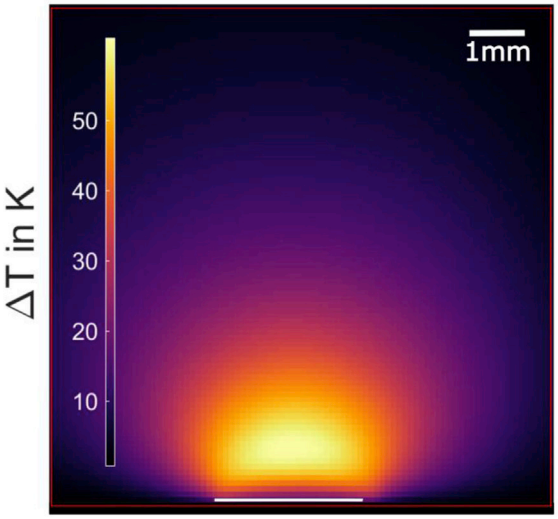

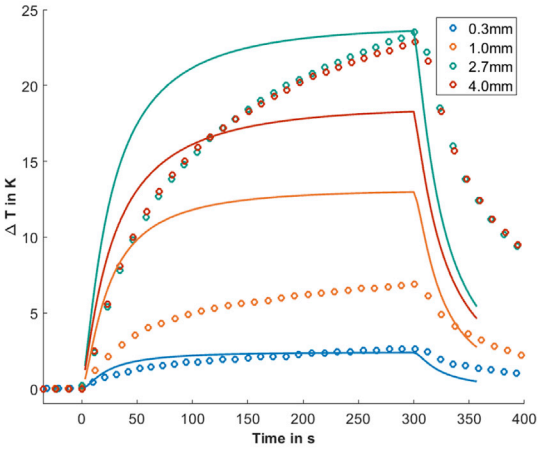

References

Ahmadi, E., Katnani, H.A., Daftari Besheli, L., Gu, Q., Atefi, R., Villeneuve, M.Y., Eskandar, E., Lev, M.H., Golby, A.J., Gupta, R., Bonmassar, G., 2016. An electrocorticography grid with conductive nanoparticles in a polymer thick film on an organic substrate improves CT and MR imaging. Radiology 280, 595–601. https://doi.org/10.1148/radiol.2016142529.

ASTM International, West Conshohocken, 2011. ASTM 2182-11a, Standard Test Method for Measurement of Radio Frequency Induced Heating Near Passive Implants during Magnetic Resonance Imaging. 2011. ASTM Int. https://doi.org/10.1520/F2182-11A.1.7.

Behrend, M.R., Ahuja, A.K., Weiland, J.D., 2008. Dynamic current density of the disk electrode double-layer. IEEE Trans. Biomed. Eng. 55, 1056–1062. https://doi.org/10.1109/TBME.2008.915723.

Bhattacharyya, A., Klapperich, C.M., 2007. Mechanical and chemical analysis of plasma and ultraviolet-ozone surface treatments for thermal bonding of polymeric microfluidic devices. Lab Chip 7, 876–882. https://doi.org/10.1039/b700442g.

Boehler, C., Stieglitz, T., Asplund, M., 2015. Nanostructured platinum grass enables superior impedance reduction for neural microelectrodes. Biomaterials 67, 346–353. https://doi.org/10.1016/j.biomaterials.2015.07.036.

Bottomley, P.A., Kumar, A., Edelstein, W.A., Allen, J.M., Karmarkar, P.V., 2010. Designing passive MRI-safe implantable conducting leads with electrodes. Med. Phys. 37, 3828–3843. https://doi.org/10.1118/1.3439590.

Boucousis, S.M., Beers, C. a., Cunningham, C.J.B., Gaxiola-Valdez, I., Pittman, D.J., Goodyear, B.G., Federico, P., 2012. Feasibility of an intracranial EEG–fMRI protocol at 3T: risk assessment and image quality. Neuroimage 63, 1237–1248. https://doi.org/10.1016/j.neuroimage.2012.08.008.

Buchenberg, W.B., Dadakova, T., Groebner, J., Bock, M., Jung, B., 2015. Comparison of two fiber-optical temperature measurement systems in magnetic fields up to 9.4 Tesla. Magn. Reson. Med. 73, 2047–2051. https://doi.org/10.1002/mrm.25314.

Carmichael, D.W., Pinto, S., Limousin-Dowsey, P., Thobois, S., Allen, P.J., Lemieux, L., Yousry, T., Thornton, J.S., 2007. Functional MRI with active, fully implanted, deep brain stimulation systems: safety and experimental confounds. Neuroimage 37, 508–517. https://doi.org/10.1016/j.neuroimage.2007.04.058.

Carmichael, D.W., Thornton, J.S., Rodionov, R., Thornton, R., McEvoy, A., Allen, P.J., Lemieux, L., 2008. Safety of localizing epilepsy monitoring intracranial electroencephalograph electrodes using MRI: radiofrequency-induced heating. J. Magn. Reson. Imaging 28, 1233–1244. https://doi.org/10.1002/jmri.21583.

Carmichael, D.W., Thornton, J.S., Rodionov, R., Thornton, R., McEvoy, A.W., Ordidge, R.J., Allen, P.J., Lemieux, L., 2010. Feasibility of simultaneous intracranial EEG-fMRI in humans: a safety study. Neuroimage 49, 379–390. https://doi.org/10.1016/j.neuroimage.2009.07.062.

Chang, E.F., 2015. Towards large-scale, human-based, mesoscopic neurotechnologies. Neuron 86, 68–78. https://doi.org/10.1016/j.neuron.2015.03.037.

Ciumas, C., Schaefers, G., Bouvard, S., Tailhades, E., Perrin, E., Comte, J.-C., Canet-Soulas, E., Bonnet, C., Ibarrola, D., Polo, G., Moya, J., Beuf, O., Ryvlin, P., 2014. A phantom and animal study of temperature changes during fMRI with intracerebral depth electrodes. Epilepsy Res. 108, 57–65. https://doi.org/10.1016/j.eplepsyres.2013.10.016.

Cogan, S.F., 2008. Neural stimulation and recording electrodes. Annu. Rev. Biomed. Eng. 10, 275–309. https://doi.org/10.1146/annurev.bioeng.10.061807.160518.

Collins, C.M., Liu, W., Wang, J., Gruetter, R., Vaughan, J.T., Ugurbil, K., Smith, M.B., 2004. Temperature and SAR Calculations for a Human Head within Volume and Surface Coils at 64 and 300 MHz 19, pp. 650–656. https://doi.org/10.1002/jmri.20041.

Dempsey, M.F., Condon, B., Hadley, D.M., 2001. Investigation of the factors responsible for burns during MRI. J. Magn. Reson. Imaging 13, 627–631.

Dykstra, A.R., Chan, A.M., Quinn, B.T., Zepeda, R., Keller, C.J., Cormier, J., Madsen, J.R., Eskandar, E.N., Cash, S.S., 2012. Individualized localization and cortical surface-based registration of intracranial electrodes. Neuroimage 59, 3563–3570. https://doi.org/10.1016/j.neuroimage.2011.11.046.

Ehses, P., Fidler, F., Nordbeck, P., Pracht, E.D., Warmuth, M., Jakob, P.M., Bauer, W.R., 2008. MRI thermometry: fast mapping of RF-induced heating along conductive wires. Magn. Reson. Med. 60, 457–461. https://doi.org/10.1002/mrm.21417.

Erhardt, J.B., Fuhrer, E., Gruschke, O.G., Leupold, J., Wapler, M.C., Hennig, J., Stieglitz, T., Korvink, J.G., 2018. Should patients with brain implants undergo MRI? J. Neural Eng. 15. https://doi.org/10.1088/1741-2552/aab4e4.

Eryaman, Y., Akin, B., Atalar, E., 2011. Reduction of implant RF heating through modification of transmit coil electric field. Magn. Reson. Med. 65, 1305–1313. https://doi.org/10.1002/mrm.22724.

Eryaman, Y., Guerin, B., Akgun, C., Herraiz, J.L., Martin, A., Torrado-Carvajal, A., Malpica, N., Hernandez-Tamames, J.A., Schiavi, E., Adalsteinsson, E., Wald, L.L., 2015. Parallel transmit pulse design for patients with deep brain stimulation implants. Magn. Reson. Med. 73, 1896–1903. https://doi.org/10.1002/mrm.25324.

Etezadi-Amoli, M., Stang, P., Kerr, A., Pauly, J., Scott, G., 2015. Controlling radiofrequency-induced currents in guidewires using parallel transmit. Magn. Reson. Med. 74, 1790–1802. https://doi.org/10.1002/mrm.25543.

Gabriel, S., Lau, R., Gabriel, C., 1996. The dielectric properties of biological tissues : II. Measurements in the frequency range 10 Hz to 20 GHz. Phys. Med. Biol. 41, 2251–2269. https://doi.org/10.1088/0031-9155/41/11/002.

Gupta, D., Hill, N.J., Adamo, M.A., Ritaccio, A., Schalk, G., 2014. Localizing ECoG electrodes on the cortical anatomy without post-implantation imaging. NeuroImage Clin 6, 64–76. https://doi.org/10.1016/j.nicl.2014.07.015.

Hamilton, L.S., Chang, D.L., Lee, M.B., Chang, E.F., 2017. Semi-automated anatomical labeling and inter-subject warping of high-density intracranial recording electrodes in electrocorticography. Front. Neuroinf. 11. https://doi.org/10.3389/fninf.2017.00062.

Hawsawi, H.B., Carmichael, D.W., Lemieux, L., 2017. Safety of simultaneous scalp or intracranial EEG during MRI: a review. Front. Physiol. 5, 42. https://doi.org/10.3389/fphy.2017.00042.

Henderson, J.M., Tkach, J., Phillips, M., Baker, K., Shellock, F.G., Rezai, A.R., 2005. Permanent neurological deficit related to magnetic resonance imaging in a patient with implanted deep brain stimulation electrodes for Parkinson's disease: case report. Neurosurgery 57, E1063. https://doi.org/10.1227/01.NEU.0000180810.16964.3E.

Hermes, D., Miller, K.J., Noordmans, H.J., Vansteensel, M.J., Ramsey, N.F., 2010. Automated electrocorticographic electrode localization on individually rendered brain surfaces. J. Neurosci. Methods 185, 293–298. https://doi.org/10.1016/j.jneumeth.2009.10.005.

ISO, T.S., 2012. 10974: assessment of the safety of magnetic resonance imaging for patients with an active implantable medical device. Geneva. Switz. Int. Organ. Stand.

Jackson, J.D., 2012. Classical Electrodynamics. John Wiley & Sons.

Jiang, T., Jiang, T., Wang, T., Mei, S., Liu, Q., Yunlin, L., Prabhu, S., Wang, X., Prabhu, S., Sha, Z., Ince, N.F., 2017. Investigation of the spatial and spectral patterns of hand extension/flexion using high-density ECoG. IEEE Trans. Neural Syst. Rehabil. Eng. 25, 370–379. https://doi.org/10.1109/NER.2015.7146691.

Jiang, T., Liu, S., Pellizzer, G., Aydoseli, A., Karamursel, S., Sabanci, P.A., Sencer, A., Gurses, C., Ince, N.F., 2018. Characterization of hand clenching in human sensorimotor cortex using high-, and ultra-high frequency band modulations of electrocorticogram. Front. Neurosci. 12. https://doi.org/10.3389/fnins.2018.00110.

Kainz, W., Neubauer, G., Überbacher, R., Alesch, F., Chan, D.D., 2002. Temperature measurement on neurological pulse generators during MR scans. Biomed. Eng. Online 1, 1–8. https://doi.org/https://doi.org/10.1186/1475-925X-1-2.

Kemler, M.A., Barendse, G.A., Van Kleef, M., de Vet, H.C., Rijks, C.P., Furnee, C.A., Van Den Wilendenberg, F.A., 2000. Spinal cord stimulation in patients with chronic reflex sympathetic dystrophy. N. Engl. J. Med. 343, 618–624.

Krafft, A., Müller, S., Umathum, R., Semmler, W., Bock, M., 2006. B1 field-insensitive transformers for RF-safe transmission lines. Magn. Reson. Mater. Physics, Biol. Med. 19, 257–266. https://doi.org/10.1007/s10334-006-0055-x.

Ladd, M.E., Quick, H.H., 2000. Reduction of resonant RF heating in intravascular catheters using coaxial chokes. Magn. Reson. Med. 43, 615–619. https://doi.org/10.1002/(SICI)1522-2594(200004)43:4<615::AID-MRM19>3.0.CO;2-B.

Langman, D.A., Goldberg, I.B., Finn, J.P., Ennis, D.B., 2011. Pacemaker lead tip heating in abandoned and pacemaker-attached leads at 1.5 tesla MRI. J. Magn. Reson. Imaging 33, 426–431. https://doi.org/10.1002/jmri.22463.

Mattei, E., Triventi, M., Calcagnini, G., Censi, F., Kainz, W., Bassen, H.I., Bartolini, P., 2007. Temperature and SAR measurement errors in the evaluation of metallic linear structures heating during MRI using fluoroptic® probes. Phys. Med. Biol. 52, 1633–1646. https://doi.org/10.1088/0031-9155/52/6/006.

Mattei, E., Triventi, M., Calcagnini, G., Censi, F., Kainz, W., Mendoza, G., Bassen, H.I., Bartolini, P., 2008. Complexity of MRI induced heating on metallic leads: experimental measurements of 374 configurations. Biomed. Eng. Online 7, 11. https://doi.org/10.1186/1475-925X-7-11.

Min, H.K., Hwang, S.C., Marsh, M.P., Kim, I., Knight, E., Striemer, B., Felmlee, J.P., Welker, K.M., Blaha, C.D., Chang, S.Y., Bennet, K.E., Lee, K.H., 2012. Deep brain stimulation induces BOLD activation in motor and non-motor networks: an fMRI comparison study of STN and EN/GPi DBS in large animals. Neuroimage 63, 1408–1420. https://doi.org/10.1016/j.neuroimage.2012.08.006.

Muller, L., Felix, S., Shah, K.G., Lee, K., Pannu, S., Chang, E.F., 2016. Thin-film , high-density micro-electrocorticographic decoding of a human cortical gyrus. 2016 38th. Annu. Int. Conf. IEEE Eng. Med. Biol. Soc. 1528–1531. https://doi.org/10.1109/EMBC.2016.7591001.

Neufeld, E., Kühn, S., Szekely, G., Kuster, N., 2009. Measurement, simulation and uncertainty assessment of implant heating during MRI. Phys. Med. Biol. Phys. Med. Biol 54, 4151–4169. https://doi.org/10.1088/0031-9155/54/13/012.

Nitz, W.R., Oppelt, A., Renz, W., Manke, C., Lenhart, M., Link, J., 2001. On the heating of linear conductive structures as guide wires and catheters in interventional MRI. J. Magn. Reson. Imaging 13, 105–114. https://doi.org/10.1002/1522-2586(200101)13:1<105::AID-JMRI1016>3.0.CO;2-0.

Nordbeck, P., Fidler, F., Weiss, I., Warmuth, M., Friedrich, M.T., Ehses, P., Geistert, W., Ritter, O., Jakob, P.M., Ladd, M.E., Quick, H.H., Bauer, W.R., 2008. Spatial distribution of RF-induced E-fields and implant heating in MRI. Magn. Reson. Med. 60, 312–319. https://doi.org/10.1002/mrm.21475.

Nordbeck, P., Weiss, I., Ehses, P., Ritter, O., Warmuth, M., Fidler, F., Herold, V., Jakob, P.M., Ladd, M.E., Quick, H.H., Bauer, W.R., 2009. Measuring RF-induced currents inside implants: impact of device configuration on MRI safety of cardiac pacemaker leads. Magn. Reson. Med. 61, 570–578. https://doi.org/10.1002/mrm.21881.

Nyenhuis, J.A., Park, Sung-Min, Kamondetdacha, R., Amjad, A., Shellock, F.G., Rezai, A.R., 2005. MRI and implanted medical devices: basic interactions with an emphasis on heating. IEEE Trans. Device Mater. Reliab. 5, 467–480. https://doi.org/10.1109/TDMR.2005.859033.

Ordonez, J., Schuettler, M., Boehler, C., Boretius, T., Stieglitz, T., 2012. Thin films and microelectrode arrays for neuroprosthetics. MRS Bull. 37, 590–598. https://doi.org/10.1557/mrs.2012.117.

Özen, A.C., 2013. A Method of Decoupling of Radio Frequency Coils in Magnetic Resonance Imaging: Application to MRI with Ultra Short Echo Time Concurrent Excitation and Acquisition. Bilkent University.

Özen, A.C., Lottner, T., Bock, M., 2019. Safety of active catheters in MRI: termination impedance versus RF-induced heating. Magn. Reson. Med. 81, 1412–1423.

Park, S.M., Nyenhuis, J.A., Smith, C.D., Lim, E.J., Foster, K.S., Baker, K.B., Hrdlicka, G., Rezai, A.R., Ruggieri, P., Sharan, A., Shellock, F.G., Stypulkowski, P.H., Tkach, J., 2003. Gelled versus nongelled phantom material for measurement of MRI-induced temperature increases with bioimplants. IEEE Trans. Magn. 39, 3367–3371. https://doi.org/10.1109/TMAG.2003.816259.

Pirotte, B.J., Voordecker, P., Levivier, M., Baleriaux, D., 2009. Principles of surgical implantation and complication avoidance. In: Canavero, S. (Ed.), Textbook of Therapeutic Cortical Stimulation. Nova Biomedical Books, New York, NY, New York, pp. 33–44.

Quesson, B., de Zwart, J.A., Moonen, C.T.W., 2000. Magnetic resonance temperature imaging for guidance of thermotherapy. J. Magn. Reson. Imaging 12, 525–533. https://doi.org/10.1002/1522-2586(200010)12:4%3e;525::AID-JMRI3>3.0.CO;2-V.

Reiss, S., Bitzer, A., Bock, M., 2015. An optical setup for electric field measurements in MRI with high spatial resolution. Phys. Med. Biol. 60, 4355–4370. https://doi.org/10.1088/0031-9155/60/11/4355.

Rubinstein, J.T., Spelman, F.A., Soma, M., Suesserman, M.F., 1987. Current density profiles of surface mounted and recessed electrodes for neural prostheses. IEEE Trans. Biomed. Eng. BME- 34, 864–875. https://doi.org/10.1109/TBME.1987.326007.

Saitoh, Y., Koichi, H., 2009. From localization to surgical implantation. In: Canavero, S. (Ed.), Textbook of Therapeutic Cortical Stimulation. Nova Biomedical Books, New York, NY, New York, pp. 17–32.

Schuettler, M., Stiess, S., King, B.V., Suaning, G.J., 2005. Fabrication of implantable microelectrode arrays by laser cutting of silicone rubber and platinum foil. J. Neural Eng. 2, S121–S128. https://doi.org/10.1088/1741-2560/2/1/013.

Shellock, F.G., 2000. Radiofrequency energy-induced heating during MR procedures: a review. J. Magn. Reson. Imaging 12, 30–36. https://doi.org/10.1002/1522-2586(200007)12:1<30::AID-JMRI4>3.0.CO;2-S.

Shellock, F.G., 2007. Comments on MR heating tests of critical implants. J. Magn. Reson. Imaging 26, 1182–1185. https://doi.org/10.1002/jmri.21176.

Spiegel, J., Fuss, G., Backens, M., Reith, W., Magnus, T., Becker, G., Moringlane, J.-R., Dillmann, U., 2003. Transient dystonia following magnetic resonance imaging in a patient with deep brain stimulation electrodes for the treatment of Parkinson disease. Case report. J. Neurosurg. 99, 772–774. https://doi.org/10.3171/jns.2003.99.4.0772.

Stieglitz, T., Rubehn, B., Henle, C., Kisban, S., Herwik, S., Ruther, P., Schuettler, M., 2009. Brain–computer interfaces: an overview of the hardware to record neural signals from the cortex. In: Progress in Brain Research. Elsevier, pp. 297–315. https://doi.org/10.1016/S0079-6123(09)17521-0.

Suesserman, M.F., Spelman, F.A., Rubinstein, J.T., 1991. In vitro measurement and characterization of current density profiles produced by nonrecessed, simple recessed, and radially varying recessed stimulating electrodes. IEEE Trans. Biomed. Eng. 38, 401–408. https://doi.org/10.1109/10.81558.

Thornton, J.S., 2017. Technical challenges and safety of magnetic resonance imaging with in situ neuromodulation from spine to brain. Eur. J. Paediatr. Neurol. 21, 232–241. https://doi.org/10.1016/j.ejpn.2016.06.001.

Vajari, D.A., Vomero, M., Erhardt, J.B., Sadr, A., Ordonez, J.S., Coenen, V.A., Stieglitz, T., 2018. Micromachines Integrity Assessment of a Hybrid DBS Probe that Enables Neurotransmitter Detection Simultaneously to Electrical Stimulation and Recording 1–15. https://doi.org/10.3390/mi9100510.

van Rhoon, G.C., Samaras, T., Yarmolenko, P.S., Dewhirst, M.W., Neufeld, E., Kuster, N., 2013. CEM43°C thermal dose thresholds: a potential guide for magnetic resonance radiofrequency exposure levels? Eur. Radiol. 23, 2215–2227. https://doi.org/10.1007/s00330-013-2825-y.

Wang, Z., Lin, J.C., Mao, W., Liu, W., Smith, M.B., Collins, C.M., 2007. SAR and temperature: simulations and comparison to regulatory limits for MRI. J. Magn. Reson. Imaging 26, 437–441. https://doi.org/10.1002/jmri.20977.

Yang, A.I., Wang, X., Doyle, W.K., Halgren, E., Carlson, C., Belcher, T.L., Cash, S.S., Devinsky, O., Thesen, T., 2012. Localization of dense intracranial electrode arrays using magnetic resonance imaging. Neuroimage 63, 157–165. https://doi.org/10.1016/j.neuroimage.2012.06.039.

Yeramian, A.K., Haas, M., Zaitsev, M., Cocosco, C.A., Korvink, J.G., Hennig, J., 2013. Generating anatomical human head model for specific absorption rate estimation in parallel MR excitation. Proc. ISMRM 21, 289.

Yeung, C.J., Susil, R.C., Atalar, E., 2002. RF safety of wires in interventional MRI: using a safety index. Magn. Reson. Med. 47, 187–193. https://doi.org/10.1002/mrm.10037.

Zijlmans, M., Worrell, G.A., Dümpelmann, M., Stieglitz, T., Barborica, A., Heers, M., Ikeda, A., Usui, N., Le Van Quyen, M., 2017. How to record high-frequency oscillations in epilepsy: a practical guideline. Epilepsia 58, 1305–1315. https://doi.org/10.1111/epi.13814.